

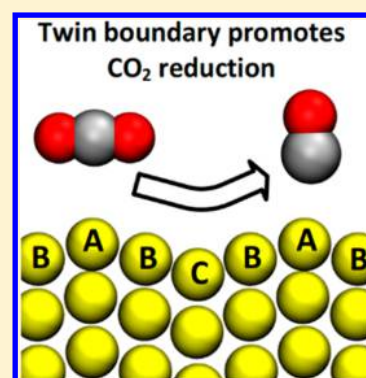
Predicted Structures of the Active Sites Responsible for the Improved Reduction of Carbon Dioxide by Gold Nanoparticles

Tao Cheng,^{ID} Yufeng Huang, Hai Xiao,^{ID} and William A. Goddard, III*^{ID}

Materials and Process Simulation Center (MSC) and Joint Center for Artificial Photosynthesis (JCAP), California Institute of Technology, Pasadena, California 91125, United States

S Supporting Information

ABSTRACT: Gold (Au) nanoparticles (NPs) are known experimentally to reduce carbon dioxide (CO₂) to carbon monoxide (CO), with far superior performance to Au foils. To obtain guidance in designing improved CO₂ catalysts, we want to understand the nature of the active sites on Au NPs. Here, we employed multiscale atomistic simulations to computationally synthesize and characterize a 10 nm thick Au NP on a carbon nanotube (CNT) support, and then we located active sites from quantum mechanics (QM) calculations on 269 randomly selected sites. The standard scaling relation is that the formation energy of *COOH (ΔE_{*COOH}) is proportional to the binding energy of *CO ($E_{*CO}^{binding}$); therefore, decreasing ΔE_{*COOH} to boost the CO₂ reduction reaction (CO₂RR) causes an increase of $E_{*CO}^{binding}$ that retards CO₂RR. We show that the NPs have superior CO₂RR because there are many sites at the twin boundaries that significantly break this scaling relation.



There is great interest in remediating the rapid increase of atmospheric carbon dioxide (CO₂) concentration with its associated increase in global temperature.¹ One strategy is to develop improved catalysts for the electrochemical reduction of CO₂ to value-added chemicals, such as carbon monoxide (CO), methane (CH₄), ethylene (C₂H₄), and ethanol (C₂H₅OH).^{2,3}

Of the metals known to reduce CO₂ to CO efficiently, gold (Au) exhibits the highest activity and selectivity among polycrystalline metals. As first reported by Hori et al.,⁴ the Faradaic efficiency for CO formation is 91% at −1.10 V vs a normal hydrogen electrode (NHE) [or −0.69 V vs reversible hydrogen electrode (RHE)] with a partial current density of 3.7 mA cm^{−2}. Moreover, Au nanoparticles (NPs) have been shown to improve the CO₂RR performance further. For example, Chen et al. reported that a Au NP derived from Au oxide films results in CO₂RR to CO with Faraday efficiency more than 60% at overpotentials as low as 0.14 V (−0.25 V vs RHE).⁵ Feng et al. found a linear relationship between CO₂RR performance and the density of grain boundaries (GBs) in NPs,⁶ concluding that the presence of GBs on Au NPs is responsible for the improved CO₂RR performance. In addition, Zhu et al. concluded that for crystalline Au NPs edge sites are the active sites for CO₂RR.^{7,8} They also showed that the size of the Au NPs is critical for controlling reaction rates; 8 nm Au NPs exhibit the best CO₂RR performance,⁷ while NPs below 2 nm are active only for hydrogen evolution reactions (HERs).⁹ Of course, the applied electric field and the electrolyte can also influence CO₂RR. Using Au nanoneedles as catalysts, Liu et al. confirm that a field-induced 20-fold increased surface-adsorbed K⁺ ion concentration enables CO₂RR to proceed with a partial current density for CO of 22 mA cm^{−2} at −0.35 V (RHE), the

best experimental results reported.¹⁰ Alloying Au¹¹ and suppressing HER¹² are other directions to improve CO₂RR.

Resolving the atomic structure of active sites responsible for the improved performance of Au NPs should provide clues helpful in designing improved CO₂RR catalysts. However, detection of the active sites directly from experiment has not been possible. We report here computer simulation experiments aimed at synthesizing, characterizing, and resolving the active sites for CO₂RR on Au NP.

First, we computationally mimic the experimental chemical vapor deposition (CVD) of a 10 nm Au NP on 44.28 nm long, 8.39 nm diameter multiwall carbon nanotube (CNT) support. Here we carried out reactive molecular dynamics (RMD) simulations of Au deposition on a 10 nm diameter CNT using the embedded-atom model (EAM) to describe the Au–Au interactions.¹³ The CVD experiments use an e-beam evaporated Au source, which we mimic by adding Au atoms into the simulation cell with a deposition rate of 3.0 Å ns^{−1} for 35 ns (the experiment deposition rate is 2 Å s^{−1} for 50 s).

We observed the rapid development of supersaturated Au vapor that in 0.3 ns began to condense. As the concentration of Au vapor reached 0.5 Au atom/nm³, we observed the formation of Au nuclei containing ~18 atoms on the CNT surface that grew quickly in various directions until their boundaries met. After 35 ns, we obtained a coarse Au NP on the CNT with a nominal thickness of about 10 nm, which is consistent with the size of the experimental catalyst.

Received: May 29, 2017

Accepted: July 4, 2017

Published: July 4, 2017



Then, we employed simulated annealing to heal the defects arising from the fast deposition rate. The peak temperature in the simulated annealing was 1164 K (100 K higher than the experimental melting point of Au metal). Each annealing cycle contained a 10 ps heating ramp from 300 to 1164 K followed by a 5 ps NVT simulation at 1164 K and then a 10 ps cooling ramp from 1164 to 300 K. Finally, we carried out a 15 ps NVT simulation at 300 K. After 120 such annealing cycles, we found that all GBs disappeared to form a single fully crystallized Au NP. From the annealing trajectories, we extracted a Au NP structure that most closely resembled the experimental catalyst (after 63 annealing cycles).

To further refine the Au NP structure and the interface between the Au NP and the CNT support, we carried out 20 ps of reactive dynamics at 300 K using the ReaxFF reactive force field trained to reproduce the equation of state of a Au FCC metal and the geometry of graphene on the Au(111) surface.¹⁴ Finally, we removed undercoordinated Au atoms (with coordination number less than five) expected to be washed away under the experimental conditions. The final Au NP structure consisted of 211 619 atoms (43 200 carbon atoms + 168 419 Au atoms) with a nominal thickness of 10 nm, as shown in Figure 1A.

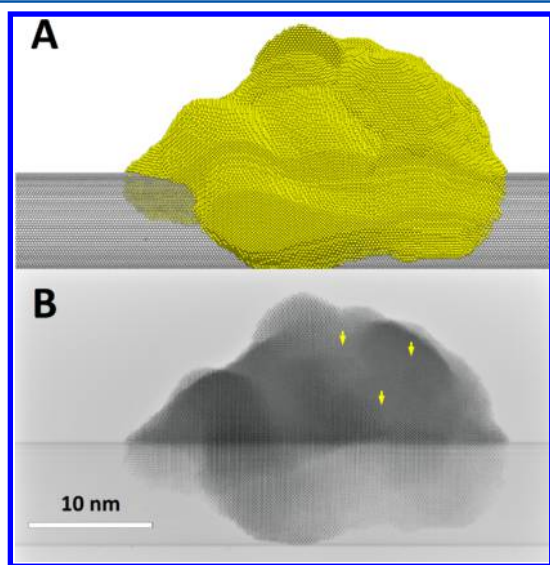


Figure 1. (A) Atomic structure of the Au NP “synthesized” computationally by simulating the CVD experiment. (B) Predicted transmission electron microscopy (TEM) images of the predicted Au NP. The yellow markers label three of the GBs.

This NP leads to an X-ray powder diffraction (XRD) pattern (see Figure S1) showing the typically broadened diffraction peaks of FCC Au due to the small grains, which is consistent with experiment. Our predicted TEM images (Figure 1B) show the GBs in the Au NP, while our dislocation analysis reveals that $1/6\langle 112 \rangle$ Shockley partial dislocations are the most abundant, leading to stacking faults on the surface. The total length of this dislocation is 3224 Å, which corresponds to a GB density of $224 \mu\text{m}^{-1}$ (as defined experimentally).¹⁵ The XRD pattern and TEM images confirm that the simulated Au NP structure is consistent with experiment.

In our previous work¹⁶ and research from other groups,^{17–19} the reaction mechanism of CO_2RR to CO on copper (Cu) is as follows:



In this pathway, physisorbed linear CO_2 [I-CO_2] was first reduced to chemisorbed CO_2 ($b\text{-CO}_2^{\delta-}$) facilitated by partial electron transfer ($\delta\text{-e}^-$). In our previous work using PBE-D3 density functional theory (DFT) calculations on the Cu(100) surface with five layers of H_2O , we found that $b\text{-CO}_2^{\delta-}$ is in a mixed coordination structure with one C–O bond (1.33 Å) parallel to the surface and one bond (1.29 Å) tilted by $\sim 60^\circ$.¹⁶ These distances are close to the C–O bond (1.26) of free CO_2 . The following proton-coupled electron transfer [$(1 - \delta)\text{-e}^-$] reaction leads to $*\text{COOH}$ formation, which completes the first electron reduction reaction. The $*\text{COOH}$ dehydration reduction reaction leads to $*\text{CO}$ formation. Finally, $*\text{CO}$ desorbs and releases the reaction site, completing the catalysis cycle. In this reaction pathway, $b\text{-CO}_2^{\delta-}$ formation is the rate-determining step (RDS), and $*\text{COOH}$ formation is the potential-determining step (PDS). Therefore, we took the formation energy of the RDS ($\Delta E_{*\text{COOH}}$) as a descriptor (as previously proposed by Peterson and Nørskov)²⁰ to characterize the activity of surface sites toward CO_2RR

$$\Delta E_{*\text{COOH}} = E_{*\text{COOH}} - (E_* + E_{\text{CO}_2} + 0.5 \times E_{\text{H}_2}) \quad (2)$$

A lower $\Delta E_{*\text{COOH}}$ indicates increased CO_2RR . We also calculated the energy of CO desorption (ΔE_{CO})

$$\Delta E_{\text{CO}} = (E_* + E_{\text{CO}}) - E_{*\text{CO}} \quad (3)$$

This nonelectrochemical reaction step determines the rate of CO leaving the surface sites; a lower $\Delta E_{*\text{CO}}$ indicates a higher CO_2RR .

Thus, the binding energy of CO can be written as

$$E_{*\text{CO}}^{\text{binding}} = E_{*\text{CO}} - (E_* + E_{\text{CO}}) = -\Delta E_{*\text{CO}} \quad (4)$$

To extract the active sites on Au NPs, we randomly selected 269 sites out of 11 360 sites (2.4%) from the catalysis surface. This random sampling introduces no presumptions, ensuring that the statistical distribution represents the overall distribution of the reactive sites. We calculated $\Delta E_{*\text{COOH}}$ and ΔE_{CO} using cluster models. These cluster models were cut from the simulated NP by taking the selected sites as the center with a cutoff of 8 Å. Such an 8 Å provides a computational accuracy of 0.02 eV, which we considered as the best balance of accuracy and efficiency.

Figure 2 shows the statistical distribution of $E_{*\text{CO}}^{\text{binding}}$ of 269 surface sites ranging from -0.1 to -0.9 eV. To compare with the fully crystalline Au NP, we built a Au octahedron (shown in Figure S2) with a length of 6.93 nm (10 425 Au atoms), which consists of 2024 facet sites (87.77%), 276 edge sites (11.97%), and 6 corner sites (0.26%). The DFT CO energy changes (negative is bound), $E_{*\text{CO}}^{\text{binding}}$, are -0.42 eV for the facet site and -0.65 eV for the edge site. Taking these two energies as a reference, we fitted the CO binding energies distribution using Gaussian functions centering at -0.42 and -0.65 eV, as shown in Figure 2. This fitting indicates that the most abundant binding sites are rhombus sites [(111)-like sites] and step sites [(110)-like sites]. These predictions are consistent with experimental electrochemical surface characterizations showing that (111) and (110) facets are dominant.⁶ However, the distribution on our CVD derived Au NP is much broader than that for the polyhedron crystalline Au NP due to the additional defects created by CVD deposition (primarily GBs and twin

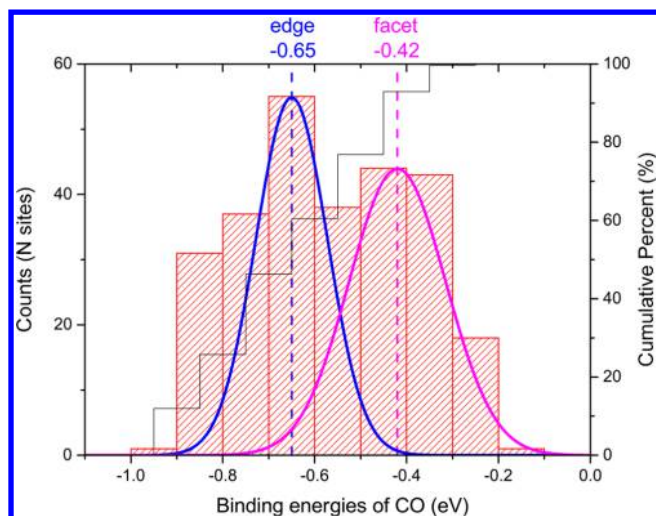


Figure 2. Distribution of CO binding energies ($E_{\text{CO}}^{\text{binding}}$, in eV) from PBE-D2 DFT on 269 Au NP surface sites selected randomly. The solid black line refers to the right axis as the cumulative percent (%). Two Gaussian functions were employed to fit the binding energies. One takes -0.65 eV (the edge site) as the center with a width of 0.077 eV (in blue), and the other takes -0.42 eV (the facet site) as the center with a width of 0.105 eV (in purple).

boundaries). This broad variation in binding site provides a site library, among which active sites exist responsible for CO_2RR .

We observed the standard scaling relation, a negative correlation between $\Delta E_{*}\text{COOH}$ and ΔE_{CO} (as shown in Figure 3), with a slope of -0.98 . These results are consistent with

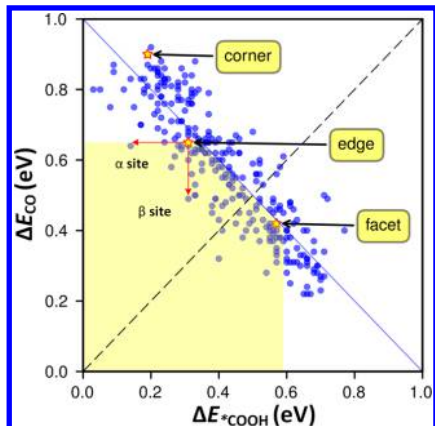


Figure 3. Reaction energy of $*\text{COOH}$ formation ($\Delta E_{*}\text{COOH}$) versus the energy of CO desorption (ΔE_{CO}). The blue circles are the results of 269 surface sites from random sampling. The yellow stars are the results of the facet, edge, and corner sites on the Au octahedron (as shown in Figure S2). The yellow filled region highlights the sites breaking the linear scaling relationship (promote CO_2RR). The red arrows highlight two sites (α site and β site) with CO_2RR performance better than that of the edge site, as predicted.

previous DFT calculations.^{21–23} Both small $\Delta E_{*}\text{COOH}$ (corresponding to a low overpotential) and ΔE_{CO} (promotes CO desorption) are favorable to promote CO_2RR . The negative correlation indicates that reduction in the overpotential (decrease of $\Delta E_{*}\text{COOH}$) occurs at the expense of increasing the CO adsorption (an increase of ΔE_{CO}). The sites with strong CO binding (large ΔE_{CO}) are also responsible for promoting the HER, therefore suppressing CO_2RR .⁹ The

optimal sites for CO_2RR are a balance between $\Delta E_{*}\text{COOH}$ and ΔE_{CO} . Experimental results suggest that edge sites provide the best balance, increasing activity for CO_2RR . Facet sites have a $\Delta E_{*}\text{COOH}$ that is too large, leading to a high overpotential, while corner sites have exhibited strong binding for $*\text{CO}$ and $*\text{H}$, which favors HER. Therefore, the surface sites responsible for promoting CO_2RR on the Au NP are expected to be those highlighted in the upper left part of Figure 3, which exhibit smaller $\Delta E_{*}\text{COOH}$ without increasing ΔE_{CO} (site α) or reducing ΔE_{CO} without increasing $\Delta E_{*}\text{COOH}$ (site β), as highlighted in Figure 3.

Therefore, these two sites should be superior in increasing CO_2RR . Figure 4C,D shows $*\text{COOH}$ and $*\text{CO}$ on the α site.

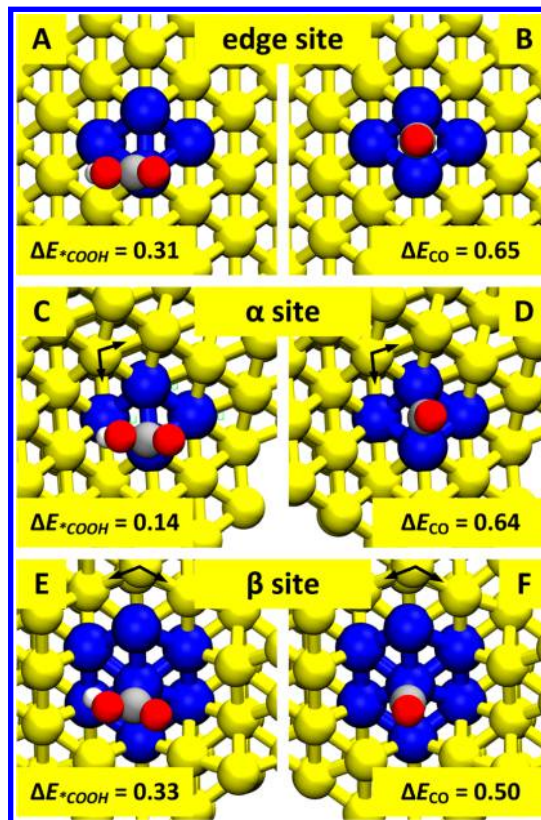


Figure 4. $*\text{CO}$ binding on the edge site (A), α site (C), and β site (E). $*\text{COOH}$ binding on the edge site (B), α site (D), and β site (F). The color key is Au in yellow, C in grey, H in white, and O in red. We highlighted the binding sites in blue for viewing convenience. Black arrows show the directions of the twin boundaries.

Figure 4E,F shows $*\text{COOH}$ and $*\text{CO}$ on the β site. The common feature of these two sites is that they are on the twin boundaries. To compare, Figure 4A,B shows $*\text{COOH}$ and $*\text{CO}$ on the edge site. The α site lies on the twin boundary, leading to a 0.17 eV decrease in $\Delta E_{*}\text{COOH}$ (0.14 eV) compared to 0.31 eV for an edge site, while ΔE_{CO} does not change (0.64 vs 0.65 eV). For the β site, the rhombus site lies on the twin boundary, leading to a 0.26 eV decrease in $\Delta E_{*}\text{COOH}$ (0.33 eV) compared with that (0.59 eV) of a facet site, which is very close to the $\Delta E_{*}\text{COOH}$ (0.31 eV) of an edge site, while ΔE_{CO} decreases by 0.14 eV (0.50 vs 0.36 eV), which is less than the increase in $\Delta E_{*}\text{COOH}$. Therefore, these surface sites on twin boundaries are superior in CO_2RR because they significantly decrease $\Delta E_{*}\text{COOH}$.

To summarize, we employed multiscale simulations to computationally “synthesize” a Au NP with a thickness of 10 nm on a CNT support. The XRD of this Au NP (Figure S1) shows the FCC crystal structure, consistent with the experimental results. The simulated TEM image (Figure 1B) shows clear GB structures. A dislocation analysis shows that 1/6<112> Shockley partial dislocations are most abundant, which induces stacking defects on the surface.

To locate the active sites for CO₂RR, we randomly selected 269 response sites out of 11 360 total sites (2.4%) for QM calculations. The QM results show a linear relationship between ΔE_{COOH} and ΔE_{CO} , showing that most sites exhibit the normal scaling relationship between *COOH stabilization, *CO desorption, and HER. However, we find a substantial fraction (10%) of NP sites on GBs or twin boundaries that significantly decrease ΔE_{COOH} without increasing ΔE_{CO} , leading to superior CO₂RR performance.

■ ASSOCIATED CONTENT

Supporting Information

The Supporting Information is available free of charge on the ACS Publications website at DOI: 10.1021/acs.jpclett.7b01335.

Simulation details, simulated XRD patterns, equation of state of FCC Au, a Au octahedral model, and ReaxFF parameters of Au and C (PDF)

■ AUTHOR INFORMATION

Corresponding Author

*E-mail: wag@wag.caltech.edu.

ORCID

Tao Cheng: 0000-0003-4830-177X

Hai Xiao: 0000-0001-9399-1584

William A. Goddard III: 0000-0003-0097-5716

Notes

The authors declare no competing financial interest.

■ ACKNOWLEDGMENTS

This work was supported by the Joint Center for Artificial Photosynthesis, a DOE Energy Innovation Hub, supported through the Office of Science of the U.S. Department of Energy under Award No. DE-SC0004993. This work used the Extreme Science and Engineering Discovery Environment (XSEDE), which is supported by National Science Foundation Grant Number ACI-1053575, and the Zwicky Astrophysics supercomputer at Caltech.

■ REFERENCES

- (1) Foster, G. L.; Royer, D. L.; Lunt, D. J. Future Climate Forcing Potentially Without Precedent in the Last 420 Million Years. *Nat. Commun.* **2017**, *8*, 14845.
- (2) Gattrell, M.; Gupta, N.; Co, A. A Review of the Aqueous Electrochemical Reduction of CO₂ to Hydrocarbons at Copper. *J. Electroanal. Chem.* **2006**, *594*, 1–19.
- (3) Kortlever, R.; Shen, J.; Schouten, K. J. P.; Calle-Vallejo, F.; Koper, M. T. M. Catalysts and Reaction Pathways for the Electrochemical Reduction of Carbon Dioxide. *J. Phys. Chem. Lett.* **2015**, *6*, 4073–4082.
- (4) Hori, Y.; Murata, A.; Kikuchi, K.; Suzuki, S. Electrochemical Reduction of Carbon Dioxides to Carbon Monoxide at a Gold Electrode in Aqueous Potassium Hydrogen Carbonate. *J. Chem. Soc., Chem. Commun.* **1987**, *10*, 728–729.
- (5) Chen, Y.; Li, C. W.; Kanan, M. W. Aqueous CO₂ Reduction at Very Low Overpotential on Oxide-Derived Au Nanoparticles. *J. Am. Chem. Soc.* **2012**, *134*, 19969–19972.

- (6) Feng, X.; Jiang, K.; Fan, S.; Kanan, M. W. Grain-Boundary-Dependent CO₂ Electroreduction Activity. *J. Am. Chem. Soc.* **2015**, *137*, 4606–4609.
- (7) Zhu, W.; Michalsky, R.; Metin, Ö.; Lv, H.; Guo, S.; Wright, C. J.; Sun, X.; Peterson, A. A.; Sun, S. Monodisperse Au Nanoparticles for Selective Electrocatalytic Reduction of CO₂ to CO. *J. Am. Chem. Soc.* **2013**, *135*, 16833–16836.
- (8) Zhu, W.; Zhang, Y.-J.; Zhang, H.; Lv, H.; Li, Q.; Michalsky, R.; Peterson, A. A.; Sun, S. Active and Selective Conversion of CO₂ to CO on Ultrathin Au Nanowires. *J. Am. Chem. Soc.* **2014**, *136*, 16132–16135.
- (9) Reske, R.; Mistry, H.; Behafarid, F.; Roldan Cuenya, B.; Strasser, P. Particle Size Effects in the Catalytic Electroreduction of CO₂ on Cu Nanoparticles. *J. Am. Chem. Soc.* **2014**, *136*, 6978–6986.
- (10) Liu, M.; Pang, Y.; Zhang, B.; De Luna, P.; Voznyy, O.; Xu, J.; Zheng, X.; Dinh, C. T.; Fan, F.; Cao, C.; et al. Enhanced Electrocatalytic CO₂ Reduction via Field-Induced Reagent Concentration. *Nature* **2016**, *537*, 382–386.
- (11) Lysgaard, S.; Myrdal, J. S. G.; Hansen, H. A.; Vegge, T. A Dft-Based Genetic Algorithm Search for AuCu Nanoalloy Electrocatalysts for CO₂ Reduction. *Phys. Chem. Chem. Phys.* **2015**, *17*, 28270–28276.
- (12) Wuttig, A.; Yaguchi, M.; Motobayashi, K.; Osawa, M.; Surendranath, Y. Inhibited Proton Transfer Enhances Au-Catalyzed CO₂-to-Fuels Selectivity. *Proc. Natl. Acad. Sci. U. S. A.* **2016**, *113*, E4585–E4593.
- (13) Foiles, S. M.; Baskes, M. I.; Daw, M. S. Embedded-Atom-Method Functions for the FCC Metals Cu, Ag, Au, Ni, Pd, Pt, and Their Alloys. *Phys. Rev. B: Condens. Matter Mater. Phys.* **1986**, *33*, 7983–7991.
- (14) Järvi, T. T.; van Duin, A. C. T.; Nordlund, K.; Goddard, W. A. Development of Interatomic Reaxff Potentials for Au–S–C–H Systems. *J. Phys. Chem. A* **2011**, *115*, 10315–10322.
- (15) Feng, X.; Jiang, K.; Fan, S.; Kanan, M. W. A Direct Grain-Boundary-Activity Correlation for CO Electroreduction on Cu Nanoparticles. *ACS Cent. Sci.* **2016**, *2*, 169–174.
- (16) Cheng, T.; Xiao, H.; Goddard, W. A. Reaction Mechanisms for the Electrochemical Reduction of CO₂ to CO and Formate on the Cu(100) Surface at 298 K from Quantum Mechanics Free Energy Calculations with Explicit Water. *J. Am. Chem. Soc.* **2016**, *138*, 13802–13805.
- (17) Luo, W.; Nie, X.; Janik, M. J.; Asthagiri, A. Facet Dependence of CO₂ Reduction Paths on Cu Electrodes. *ACS Catal.* **2016**, *6*, 219–229.
- (18) Nie, X.; Esopi, M. R.; Janik, M. J.; Asthagiri, A. Selectivity of CO₂ Reduction on Copper Electrodes: The Role of the Kinetics of Elementary Steps. *Angew. Chem., Int. Ed.* **2013**, *52*, 2459–2462.
- (19) Peterson, A. A.; Abild-Pedersen, F.; Studt, F.; Rossmeisl, J.; Nørskov, J. K. How Copper Catalyzes the Electroreduction of Carbon Dioxide into Hydrocarbon Fuels. *Energy Environ. Sci.* **2010**, *3*, 1311–1315.
- (20) Peterson, A. A.; Nørskov, J. K. Activity Descriptors for CO₂ Electroreduction to Methane on Transition-Metal Catalysts. *J. Phys. Chem. Lett.* **2012**, *3*, 251–258.
- (21) Back, S.; Kim, H.; Jung, Y. Selective Heterogeneous CO₂ Electroreduction to Methanol. *ACS Catal.* **2015**, *5*, 965–971.
- (22) Kim, K.-S.; Kim, W. J.; Lim, H.-K.; Lee, E. K.; Kim, H. Tuned Chemical Bonding Ability of Au at Grain Boundaries for Enhanced Electrochemical CO₂ Reduction. *ACS Catal.* **2016**, *6*, 4443–4448.
- (23) Back, S.; Yeom, M. S.; Jung, Y. Active Sites of Au and Ag Nanoparticle Catalysts for CO₂ Electroreduction to CO. *ACS Catal.* **2015**, *5*, 5089–5096.